

Probing Hyperbolic Shear Polaritons in β -Ga₂O₃ Nanostructures Using STEM-EELS

Zhenyu Zhang, Tao Wang,* Hailing Jiang, Ruishi Qi, Yuehui Li, Jinlin Wang, Shanshan Sheng, Ning Li, Ruochen Shi, Jiaqi Wei, Fang Liu, Shengnan Zhang, Xiaoqing Huo, Jinlong Du, Jingmin Zhang, Jun Xu, Xin Rong, Peng Gao,* Bo Shen, and Xinqiang Wang*

Phonon polaritons, quasiparticles arising from strong coupling between electromagnetic waves and optical phonons, have potential for applications in subdiffraction imaging, sensing, thermal conduction enhancement, and spectroscopy signal enhancement. A new class of phonon polaritons in low-symmetry monoclinic crystals, hyperbolic shear polaritons (HShPs), have been verified recently in β -Ga₂O₃ by free electron laser (FEL) measurements. However, detailed behaviors of HShPs in β -Ga₂O₃ nanostructures still remain unknown. Here, by using monochromatic electron energy loss spectroscopy in conjunction with scanning transmission electron microscopy, the experimental observation of multiple HShPs in β -Ga₂O₃ in the mid-infrared (MIR) and far-infrared (FIR) ranges is reported. HShPs in various β -Ga₂O₃ nanorods and a β -Ga₂O₃ nanodisk are excited. The frequency-dependent rotation and shear effect of HShPs reflect on the distribution of EELS signals. The propagation and reflection of HShPs in nanostructures are clarified by simulations of electric field distribution. These findings suggest that, with its tunable broad spectral HShPs, β -Ga₂O₃ is an excellent candidate for nanophotonic applications.

roles in the study of light–matter interaction and the fabrication of photonic devices.^[1–4] Phonon polaritons have unique advantages in the fields of subwavelength light confinement and controllable energy transfer, enabling their applications in superlensing, waveguides, and heat transfer.^[5–10] It has been found that crystal symmetry plays an important role in the excitation and propagation of phonon polaritons. In isotropic crystals with high symmetry, phonon polaritons propagate uniformly in all directions.^[1,11] Uniaxial or biaxial crystals have lower symmetry. These crystals have permittivity components with different signs along their principal directions, leading to hyperbolic light propagation. Hyperbolic phonon polaritons (HPhPs) have been found experimentally in anisotropic materials, such as h-BN^[1,12] and α -MoO₃.^[13–15] The highly directional HPhPs allow fine control of energy flow in semiconductors.^[16,17] Monoclinic crystals,

with further reduced symmetry, can also support phonon polaritons. Phonon polaritons in monoclinic β -Ga₂O₃ have been verified by the free electron laser (FEL) measurements recently.^[18]

1. Introduction

Phonon polaritons refer to the couplings between photons and optical phonons in polar crystals, therefore, they play important

Z. Zhang, T. Wang, H. Jiang, J. Wang, S. Sheng, J. Wei, F. Liu, X. Rong, B. Shen, X. Wang
 State Key Laboratory for Mesoscopic Physics and Frontiers Science Center for Nano-Optoelectronics
 School of Physics
 Peking University
 Beijing 100871, China
 E-mail: cwwangtao@pku.edu.cn; wangshi@pku.edu.cn

Z. Zhang, T. Wang, R. Qi, Y. Li, N. Li, R. Shi, J. Du, J. Zhang, J. Xu, P. Gao
 Electron Microscopy Laboratory
 School of Physics
 Peking University
 Beijing 100871, China
 E-mail: p-gao@pku.edu.cn

 The ORCID identification number(s) for the author(s) of this article can be found under <https://doi.org/10.1002/adma.202204884>

[Correction added on March 1, 2024 after first online publication: T.W. and P.G. were made a co-corresponding author.]

DOI: 10.1002/adma.202204884

Y. Li, P. Gao
 International Center for Quantum Materials
 School of Physics
 Peking University
 Beijing 100871, China

S. Zhang, X. Huo
 The 46th Research Institute
 China Electronics Technology Group Corporation (CETC)
 Tianjin 300220, China

P. Gao, B. Shen, X. Wang
 Collaborative Innovation Center of Quantum Matter
 Peking University
 Beijing 100871, China

B. Shen, X. Wang
 Peking University Yangtze Delta Institute of Optoelectronics
 Nantong, Jiangsu 226010, China

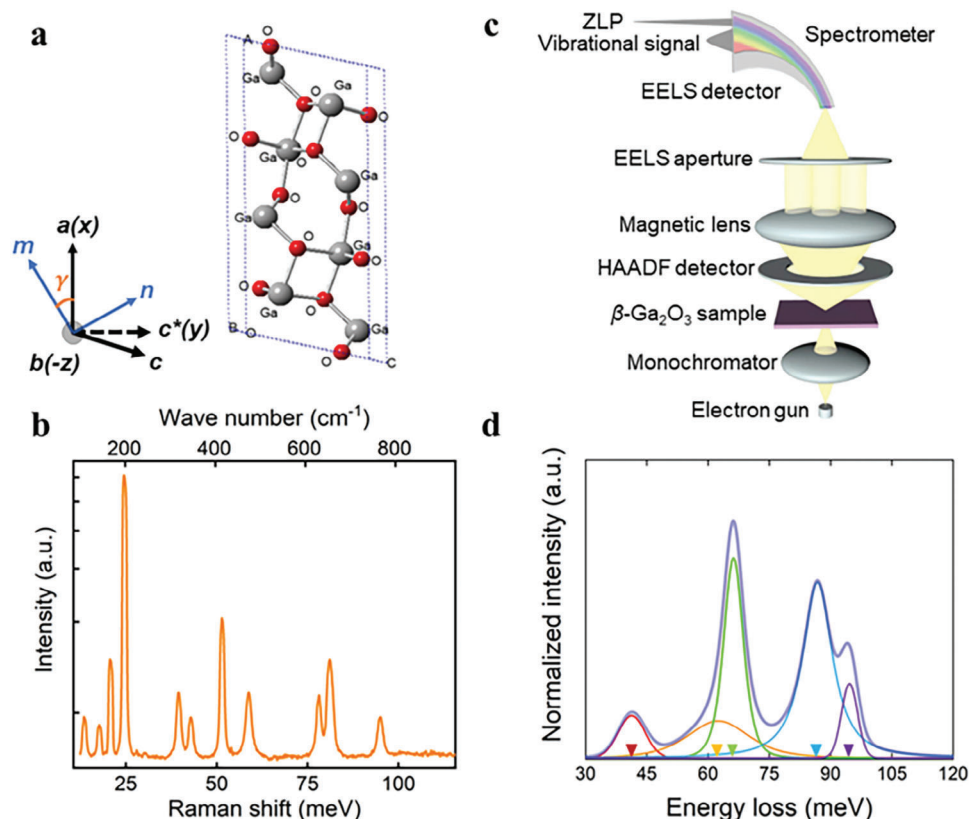


Figure 1. a) Crystal structure of β -Ga₂O₃. The crystal axes of the unit cell are also shown, along with the redefined vector c^* , the rotated coordinate system $[mnz]$, and the rotation angle γ . b) Raman spectrum of β -Ga₂O₃. A large number of scattering peaks are observed, indicating various phonon modes. c) Schematic of the STEM-EELS experimental setup. d) Electron energy loss spectrum recorded under an aloof geometry after background subtraction and deconvolution (bold blue curve) containing several energy loss peaks (thin colored curves). The positions of the peaks are indicated by small triangles.

The dispersive propagation direction and sheared isofrequency surface lead to a new class of polariton, hyperbolic shear polaritons (HShPs). Although the propagation of HShPs on the surface of β -Ga₂O₃ has been clarified, its detailed behavior, when excited in confined nanostructures, remains uninvestigated.

β -Ga₂O₃, an ultrawide-bandgap semiconductor with a bandgap of 5.04 eV,^[19–28] is an excellent candidate for power electronic devices due to its high electric breakdown field (up to ≈ 8 MV cm⁻¹).^[29–32] However, the poor thermal conductivity of β -Ga₂O₃ sabotages device performance.^[33] Theoretical studies suggested to use phonon polaritons to improve heat transfer in β -Ga₂O₃ devices by introducing a nanoscale heat channel.^[9,10] Additionally, as an anisotropic material, β -Ga₂O₃ can sustain phonon polaritons along different directions over a wide spectral range according to theoretical predictions,^[6,34] which is desirable for nanophotonic applications. Thanks to the recent development of electron energy loss spectroscopy (EELS) with support from scanning transmission electron microscopy (STEM), an electron probe with atomic spatial resolution and a sub-10 meV energy resolution, as well as an extremely wide spectral range (from ≈ 20 meV to 3 keV) can be achieved,^[35–41] making it possible to study the HShP modes of β -Ga₂O₃ in a diversity of nanostructures.

Here, using such a STEM-EELS, we study the nature of HShPs in various β -Ga₂O₃ nanostructures. By performing nu-

merical simulation of field distribution in the nanorods, we clarify the nature of polariton propagation and reflection in β -Ga₂O₃ nanorods. We then interpret the experimental EELS peaks along the nanorods as a combined effect of polaritons incident and reflected at all directions. Then we demonstrate the possibility of tuning the propagation of HShPs by changing the size of the β -Ga₂O₃ nanorods. In addition, we also excite and detect HShPs in a β -Ga₂O₃ nanodisk. The slight asymmetry of the distribution of EELS intensity indicates the broken of mirror symmetry, which originates from the shear effect of HShPs. The tunable broad spectral HShPs in β -Ga₂O₃ expand the scope of β -Ga₂O₃ from its application in traditional electronic devices to applications in nanophotonics and metamaterials.

2. Results

2.1. Structural Analysis of β -Ga₂O₃ and EELS Workflow

The unit cell of β -Ga₂O₃ is shown in **Figure 1a**. It has three types of inequivalent O atoms and two types of inequivalent Ga atoms.^[42] The inset in **Figure 1a** shows three marked crystal axes. As a feature of the monoclinic lattice, axis b is perpendicular to the ac plane, where the angle between the a axis and the c axis is larger than 90°. For convenience, we chose a new vector in the ac plane, defined as c^* , such that axes a , b , and c^*

are perpendicular to each other. Due to the low-symmetry lattice structure, β -Ga₂O₃ has a large number of phonon modes in the MIR to FIR regions, as shown in a Raman scattering spectrum in Figure 1b. According to group theory,^[43] β -Ga₂O₃ has eight pairs of TO and LO phonons that vibrate in the *ac* plane, along with four other pairs polarized along the *b* axis. Using the eigenpolarization model,^[44] we calculated the permittivity of β -Ga₂O₃ in the MIR and FIR spectral ranges. The monoclinic symmetry introduces off-diagonal terms to the permittivity tensor of β -Ga₂O₃. The understanding and management of this permittivity tensor have been discussed in detail.^[18] Here, we treat the permittivity in the same way. After diagonalizing the real part of the permittivity tensor, we get a real transformation matrix. This matrix represents a rotation in the monoclinic plane. The principal axes after rotation (*m* and *n*) and the rotation angle γ are marked in the inset of Figure 1a. Then, the β -Ga₂O₃ crystal system can be simplified into a “pseudo-biaxial” crystal with the remaining imaginary off-diagonal terms. The detailed parameters of permittivity elements can be found in Figure S1 (Supporting Information), which is a replot of the permittivity data shown in previous work.^[18] The nonvanishing off-diagonal imaginary part $\text{Im}(\epsilon_{mn})$ introduces the shear effect,^[18] which breaks the mirror symmetry of the polariton propagation. The frequency-dependent rotation of the isofrequency surface and the shear effect make the study of the polariton response in β -Ga₂O₃ more sophisticated than in any other previously reported materials.^[5–10,12–15,45]

A simplified sketch of experimental procedure is presented in Figure 1c, which shows a typical STEM-EELS workflow. High-energy electrons focus at ≈ 0.1 nm and interact with β -Ga₂O₃ to initiate phonon polaritons, from which a small amount of energy (usually tens of meV) is lost. The EELS detector records energy loss information for low-momentum transfer electrons, and thus lattice vibration data can be extracted. An example is shown in Figure 1d, which was obtained from EELS experiment on a ground β -Ga₂O₃ nanorod. The EEL spectra were recorded via an aloof geometry, which means that the electron beam is located very close to the sample but outside of it. The aloof geometry reduces the damage to the samples and increases the signal-to-noise ratio.^[13,36,46] The vibration peaks can be extracted by subtracting the background signal followed by deconvolution, which demonstrates the interactions between electrons and phonons. As shown in Figure 1d, there are five EELS peaks, i.e., those at 40, 62, 66, 86, and 94 meV, that are determined by a Gaussian fitting with multiple peaks, and their positions are indicated by solid triangles. Details of EELS data processing are discussed in the Experimental Section.

2.2. Observation of HShPs in β -Ga₂O₃ Nanorods

By emitting electrons into various β -Ga₂O₃ nanostructures, HShPs can be excited and detected. Using focused ion beam (FIB) etching, we fabricated various β -Ga₂O₃ nanorods with specific orientations and sizes.^[47,48] Details of FIB etching can be found in the Experimental Section. For example, the fabricated β -Ga₂O₃ nanorod has long and short axes along *c** and *b*, respectively. Its length, width, and thickness are ≈ 3000 , 300, and 500 nm, respectively. Electrons with high momentum transfer are collected by the annular detector at a high angle so that we

can obtain a high-angle annular dark-field scanning transmission electron microscopy (HAADF-STEM) image of the samples at an atomic spatial resolution. Figure 2a shows a HAADF-STEM image that confirms the length and width of the fabricated sample. A high-resolution HAADF-STEM image is shown in the lower right corner, where the atomic structure confirms our chosen orientation.

When a selected area near the sample is scanned (shown in the yellow dashed box in Figure 2a, and the aloof geometry is used), EELS maps can be obtained at different energies. Typical EELS maps are shown in Figure 2b. Notably, these EELS maps reflect the electromagnetic density of states (DOS) projected along the electron beam.^[49] The nodal patterns can be seen clearly in Figure 2b. The EELS peak marked by the black triangles beside the maps moves toward the terminal of the nanorod with increasing energy loss. Similar nodal patterns can be found in the cases of HPhPs in α -MoO₃ nanoribbon,^[13] which have been interpreted as interference between the incident and reflected polaritons. However, in monoclinic crystals, the direction of polariton propagation is dispersive within the monoclinic plane.^[18] This brings much complexity to the excitation and reflection analysis of phonon polaritons.

An EELS line profile showing the scanning along the *c** axis with the summed map signal along the *b* axis is presented in Figure 2c. The nodal patterns in Figure 2b correspond to the branch of peaks in the line profile at a spectral range of 70–90 meV. Modes in other spectral ranges are difficult to distinguish on the line profile, possibly due to the limited energy resolution. Therefore, our following analysis mainly focus on the 70–90 meV frequency region. To corroborate that HShPs have indeed been excited, we performed a finite-difference time-domain (FDTD) simulation^[50] using the calculated permittivity tensor of β -Ga₂O₃. The simulated line profile is shown in Figure 2d. The simulation result agrees well with our experiment.

To understand what happened at the EELS branch at 70–90 meV, we simulated the electromagnetic field in the nanorod using COMSOL Multiphysics. For example, at the energy of 80 meV, the EELS spectra show a peak when the electron beam emits 870 nm away from the nanorod terminal. This can be extracted from the EELS line profile in Figure 2c. The plot of the EELS peak is shown in Figure 3a. Then, we can propose the corresponding model of the experimental circumstance, as shown in Figure 3b. The nanorod was built with same width, thickness, and orientation as the fabricated sample shown in Figure 2. The position of the electron beam was 870 nm away from the nanorod terminal, where the experimental results show EELS peak. In addition, the electron beam was set to be 50 nm outside the nanorod to satisfy the aloof geometry. Figure 3c displays the simulated electric field distribution in the nanorod at the energy of 80 meV. The field pattern can be analyzed from two aspects. At the region of the far end of the nanorod, the tilted field distribution in *ac* plane results from the frequency-dependent rotation effect. At the region near the electron beam, the zigzag field pattern indicates the propagation and reflection of polaritons in all directions. As a comparison, we perform another simulation on the same model in Figure 3b. The only difference is that we set the off-diagonal terms of the permittivity tensor of the nanorod to be zero. Then the material of the nanorod becomes a normal hyperbolic material like α -MoO₃. The simulated electric field distribution of this

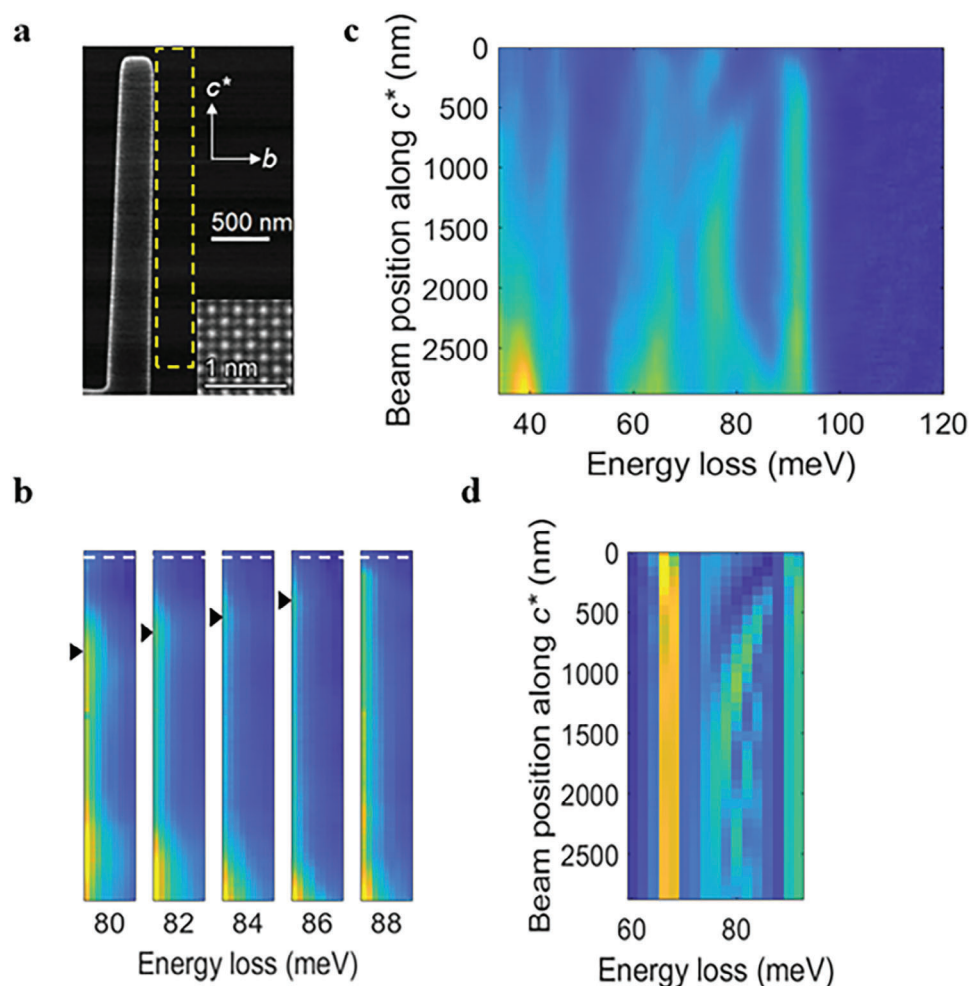


Figure 2. Excitation of HShPs in a β - Ga_2O_3 nanorod with a selected orientation. a) HAADF-STEM image of an ≈ 500 nm thick nanorod. The inset shows an atomic-resolved HAADF-STEM image of the TEM lamella-supported nanorod. The inset shows the atomic structure of β - Ga_2O_3 , which verifies the orientation of the nanorod. b) EELS maps corresponding to the yellow dashed box in (a) are shown for 80, 82, 84, 86, and 88 meV, respectively. The energy range is chosen for spatial patterns supporting polariton modes. The white dashed line marks the terminal of the nanorod. The solid black triangles on the left of each map mark the position of the first distinguishable EELS peak near the terminal. c) Experimental EELS line profile along the c^* direction obtained by integrating the EELS maps along the b axis. The origin of the vertical axis is located at the end of the nanorod. d) Simulated EELS line profile via FDTD.

model is presented in Figure 3d. At the area between electron beam and the nanorod terminal, we can find field pattern similar to that of standing wave. This pattern indicates the interference of incident and reflected polaritons, which has been discussed in the previous work of α - MoO_3 nanorods.^[13] In the aloof geometry we used here, the electron beam excite polaritons in the whole nanorod. The EELS spectrum results from the integral of all the polariton-induced energy loss. When the permittivity tensor is diagonal, the principal axis, as well as the axis of mirror symmetry is frequency-independent. For example, we can find in Figure 3d that the field distribution is basically symmetric about a and b axis. Then the field distribution of the nanorod can be approximately simplified into a one-dimensional case, making the appearance of EELS peak directly relate to the interference enhancement of polaritons along the nanorod. However, things are totally different for β - Ga_2O_3 nanorods with a nondiagonal permittivity tensor. The dispersive rotation induced in the monoclinic

plane breaks the symmetry about the crystal axes. Therefore, the maximum of EELS spectrum is no longer decided by the interference of polaritons along some specific direction. On the contrary, the EELS peak is a combined effect of polaritons incident and reflected at all directions. Thus, it is hard to give an analytical expression between the EELS peak position and the polariton excitation.

The relation between EELS spectrum and polariton excitation also suggested that the tune of phonon polaritons will be reflected in the EELS spectrum. For example, HShPs can be tuned by changing the size of nanostructures where HShPs are excited, which is common practice in previous studies of phonon polaritons in other materials.^[45,51–53] A HAADF-STEM image of three nanorods with different diameters fabricated by FIB etching is shown in Figure 4a. The widths of the nanorods are ≈ 770 , 560, 300 nm from left to right. The electron beam scan line profiles along these nanorods are compared, and the results are shown

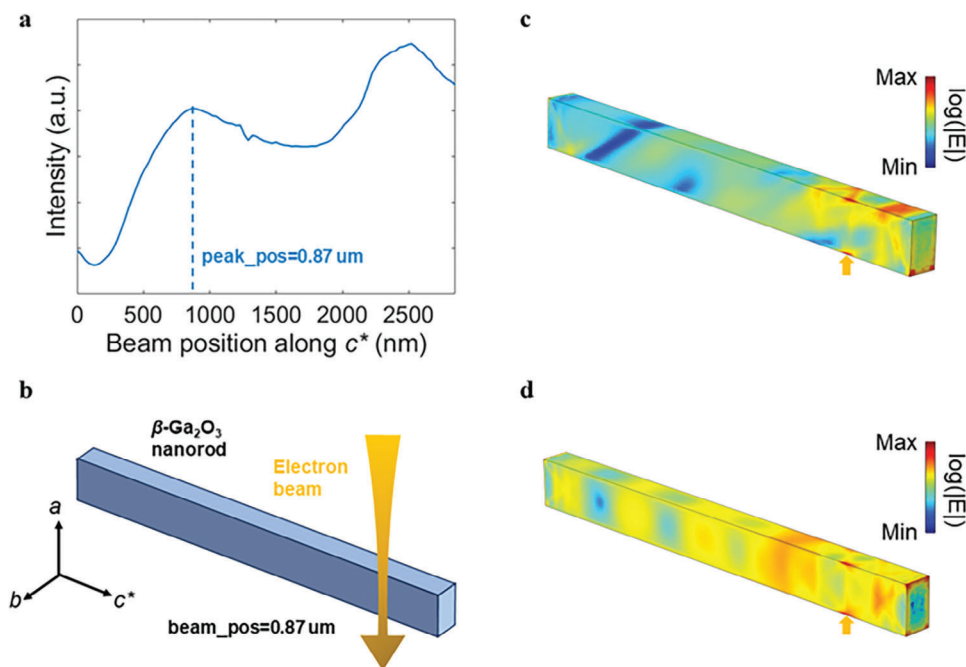


Figure 3. Simulation results for electric field in the β -Ga₂O₃ nanorod at the energy of 80 meV. a) EELS line profile extracted from Figure 2c at the energy of 80 meV. EELS peak can be found at 870 nm away from the nanorod terminal. b) Model used for simulation. The nanorod was built with same width, thickness, and orientation as the fabricated sample shown in Figure 2. The position of the electron beam was 870 nm away from the nanorod terminal, where the experimental results show EELS peak. In addition, the electron beam was set to be 50 nm outside the nanorod to satisfy the aloof geometry. c) Simulated electric field distribution in the nanorod at the energy of 80 meV under the setup in (b). Log scale was used in the colormap to get a better contrast. The position of the electron beam was marked by the yellow arrow. d) Simulated electric field distribution after setting the off-diagonal terms of the permittivity tensor of the nanorod to be zero.

in Figure 4b. The typical polariton branch at 70–90 meV can be found in all three line profiles. We can extract the position of EELS peaks along the nanorods from the EELS line profiles, and the results are shown in Figure 4c. We can see that the EELS peaks move away from the nanorod terminal when the width of the nanorods increases.

To clarify the influence of different width of nanorods on the propagation of HShPs, we performed field distribution simulation on the three nanorods in Figure 4 at the energy of 80 meV. The results are shown in Figure 5. The electron beams are placed at the positions where EELS line profiles show peaks, as extracted in Figure 4c. For nanorods with width 300, 560, and 770 nm, the electron beams are placed at 870, 1520, 1610 nm away from the nanorods terminal, respectively. The middle and right panels show the field distributions at the side and top surfaces of the nanorods. We can see that when the width of the nanorods increase, the field distributions in ac plane are approximately the same, as shown in the middle panels of Figure 5. The main difference lies on the propagation of polaritons in bc^* plane, as shown in the right panels in Figure 5. In wider nanorods, polaritons need to propagate a longer path before being reflected at the edge of the nanorods. This results in the positions of EELS peaks moving away from the nanorod terminal. The variation of EELS peaks suggests that propagation and interference of HShPs in nanorods can be continuously tunable by simply altering the size of the nanorods.

In addition, the energy ranges of the polariton branches discussed in the EELS measurement of the nanorods are ≈ 10 meV.

This energy range is comparable or even less than the spectral resolution of the EELS technique we used. The lack of energy resolution suggests that the EELS spectrum we got originates from the convolution of all polariton-related effects within the Reststrahlen band. Even some polariton-unrelated effects outside the Reststrahlen band will take into part. This means that the accurate peak position may be different from that extracted from our data. However, the qualitative conclusion about the phonon polaritons excitation in β -Ga₂O₃ nanorods is still valid. This also shows that the further investigation of HShPs in β -Ga₂O₃ nanostructures requires experimental techniques with higher energy resolution.

2.3. Observation of HShPs in β -Ga₂O₃ Nanodisk

We have illustrated the excitation and propagation of phonon polaritons in β -Ga₂O₃ nanorods via EELS experiments and simulations. It can be found that the difference compared with polaritons in nanorods with normal hyperbolic materials is mainly introduced by the frequency-dependent rotation in monoclinic plane. To investigate another important feature of HShPs, namely the shear effect, we performed EELS experiments on β -Ga₂O₃ nanostructures with another shape. Figure 6a shows the HAADF-STEM image of a β -Ga₂O₃ nanodisk in ac plane. The diameter and thickness of the nanodisk are ≈ 2000 and 500 nm, respectively. Electron beam emitted along b axis is used to scan around the nanodisk to excite HShPs. Figure 6b,c shows

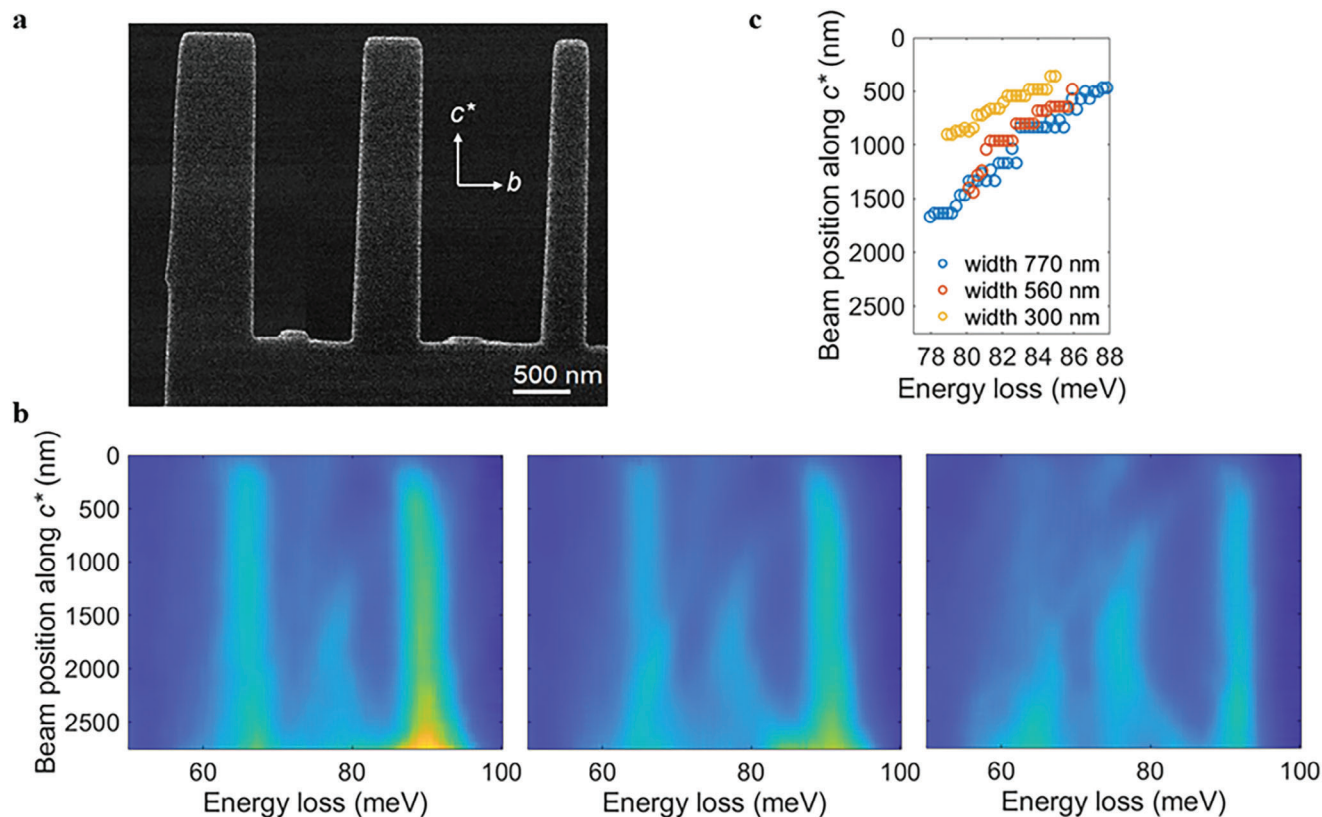


Figure 4. Nanoscale size effects on the HShPs in β -Ga₂O₃ nanorods. a) HAADF-STEM image of three nanorods with width $d = 770, 560,$ and 300 nm, respectively. The long axes of the nanorods are along c^* . b) Experimental profiles of EELS lines of the three nanorods. The line profiles from left to right correspond to $d = 770, 560, 300$ nm. The origin of the vertical axis is located at the end of the nanorod. c) The position of the EELS peak along the nanorod at the energy range of $77\text{--}89$ meV, which extracted from the EELS line profiles in (b). The blue, orange, and yellow circles correspond to the results of nanorods with width $d = 770, 560,$ and 300 nm, respectively.

the corresponding EELS maps at the energy of 62 and 80 meV, respectively. It can be found that the angular position of the maximum of EELS intensity varies with frequency. This variation in the EELS pattern also results from the frequency-dependent rotation induced by the permittivity tensor.

Furthermore, the EELS intensity adjacent to the edge of the nanodisk in the EELS maps shown in Figure 6b,c is extracted and plotted in polar coordinates. The results are shown in Figure 7a,b, respectively. The corresponding simulation results are shown in Figure 7c,d. The calculated polar plots generally agree with the experimental results. The difference results from the imperfect geometry of the nanodisk sample, as well as the influence of the handle of the nanodisk. It can be found that the EELS intensity around the nanodisk is slightly asymmetric about the angular position of the intensity maximum at both frequencies. This means that the mirror symmetry is broken, and no mirror symmetry axis can be found for the intensity distribution of the EELS maps. This symmetry-broken pattern indicates the shear effect induced by the nonvanishing off-diagonal imaginary part $\text{Im}(\epsilon_{mn})$ of the permittivity tensor. Figure 7e,f shows the simulated electric field distributions on the top surface of the nanodisk at the energy of 62 and 80 meV. The electron beam are placed at the angular position where the simulated EELS intensity in Figure 7c,d show maximum. The field distributions show that HShPs excited by the electron beam propagate and reflected at the edge of the nan-

odisk. Both field patterns form closed shapes, which indicates that the maximum of EELS intensity results from the interference enhancement of propagated and reflected polaritons. Slight asymmetry is also found in both electric field patterns. This suggests the sheared propagation of polaritons in ac plane. Therefore, the asymmetric distribution of EELS intensity just originates from the shear effect of HShPs.

3. Conclusions

In summary, we have excited and detected HShPs in β -Ga₂O₃ in the MIR and FIR ranges via STEM-EELS. Thanks to the atomic spatial resolution and sub-10-meV energy resolution, we were able to distinguish the polariton branches in EELS signals. By performing simulation of electric field distribution in nanorods, we found that the frequency-dependent rotation effect makes the polaritons propagate dispersively in the nanorods. We then interpreted EELS peaks as a combined effect of polaritons incident and reflected at all directions. We found that the excitation and propagation of HShPs in β -Ga₂O₃ nanorods can be tuned by altering the size of nanorods. Furthermore, we excited HShPs in a β -Ga₂O₃ nanodisk. The slight broken of mirror symmetry in EELS intensity distribution was found. Electric field simulations suggested that this asymmetry originates from the sheared propagation of HShPs. These findings undoubtedly

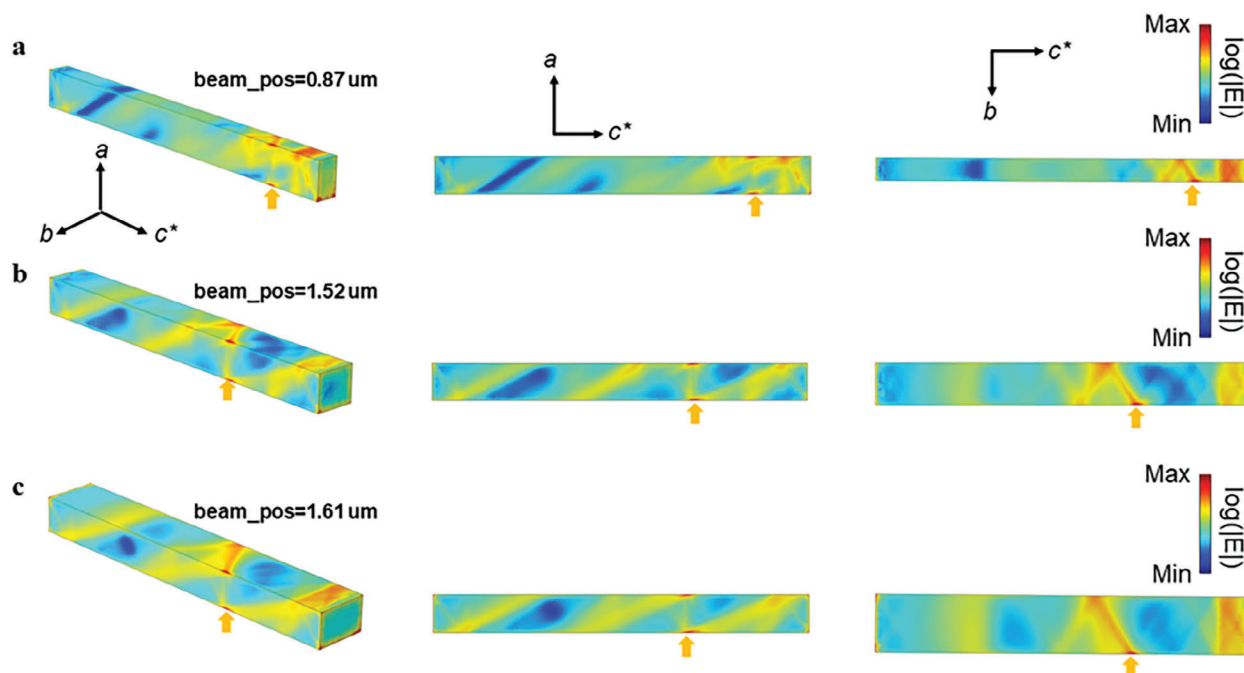


Figure 5. Simulation results for electric field distribution in β -Ga₂O₃ nanorods with different widths at the energy of 80 meV. a–c) Simulated electric field distribution in nanorods with width a) 300 nm, b) 560 nm, and c) 770 nm, respectively. The left panel shows the overall field distribution. The middle panel shows the field distribution on the side surface of the nanorods. The right panel shows the field distribution on the top surface of the nanorods. The orientation of the nanorods is marked by the inset. The positions of the electron beam are marked by the yellow arrows. Log scales are used in the colormaps to get a better contrast.

improve our understanding of β -Ga₂O₃ with regard to its excitation and propagation of vibrational modes, especially at MIR to FIR frequencies. The sustainability and tunability of the broad spectral range of HShPs in β -Ga₂O₃ makes this material a promising candidate for applications in nanophotonics.

4. Experimental Section

β -Ga₂O₃ Nanorods Fabrication: The ground β -Ga₂O₃ nanorods were derived from bulk β -Ga₂O₃. β -Ga₂O₃ was found to cleave easily on the (100) plane; when bulk β -Ga₂O₃ is milled in agate mortar, β -Ga₂O₃

nanorod forms along the *b* direction. The diameter of the β -Ga₂O₃ nanorods varied from 100 to 1000 nm. The nanorods are diluted with alcohol and dropped on a copper grid for the TEM measurement.

FIB Etching: β -Ga₂O₃ nanorods and flakes along different directions were milled by a ThermoFisher Helios G4 UX FIB system. The crystal plane was first determined by atomic-resolution HAADF-STEM, and β -Ga₂O₃ nanorods and flakes were then cut into different shapes along different crystal orientations. Final milling to the intended size was accomplished using a low ion beam current (47 pA). The image of samples fabricated by FIB is shown in Figure S2, Supporting Information.

β -Ga₂O₃ Permittivity Calculation: The permittivity of β -Ga₂O₃ is calculated by the eigenpolarization model.^[44] Free charge carrier concentration was used $N = 5 \times 10^{16} \text{ cm}^{-3}$ for the intrinsic β -Ga₂O₃ sample was used

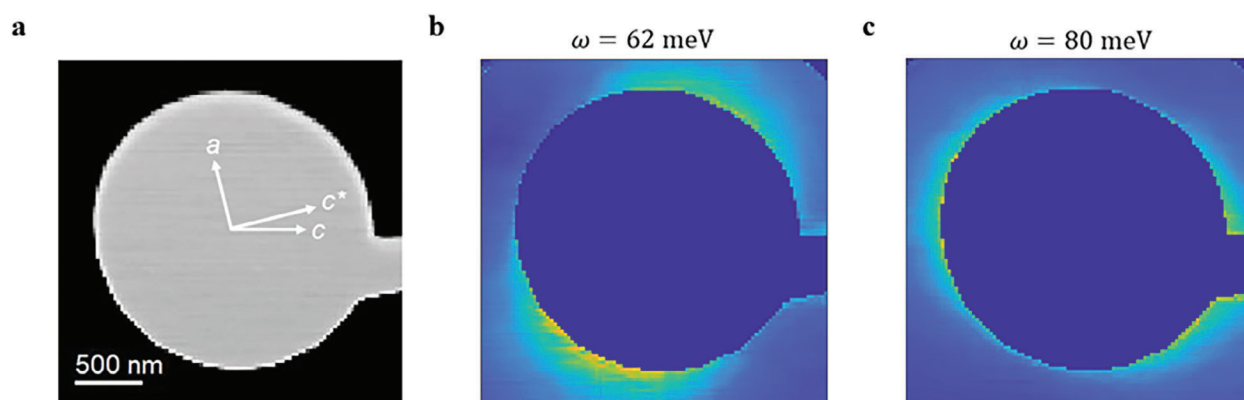


Figure 6. Excitation of HShPs in a β -Ga₂O₃ nanodisk. a) HAADF-STEM image of the β -Ga₂O₃ nanodisk with the diameter of ≈ 2000 nm. The inset shows the orientation of the disk. b,c) EELS maps around the disk shown in (a) at the energy of b) 62 meV, and c) 80 meV, respectively.

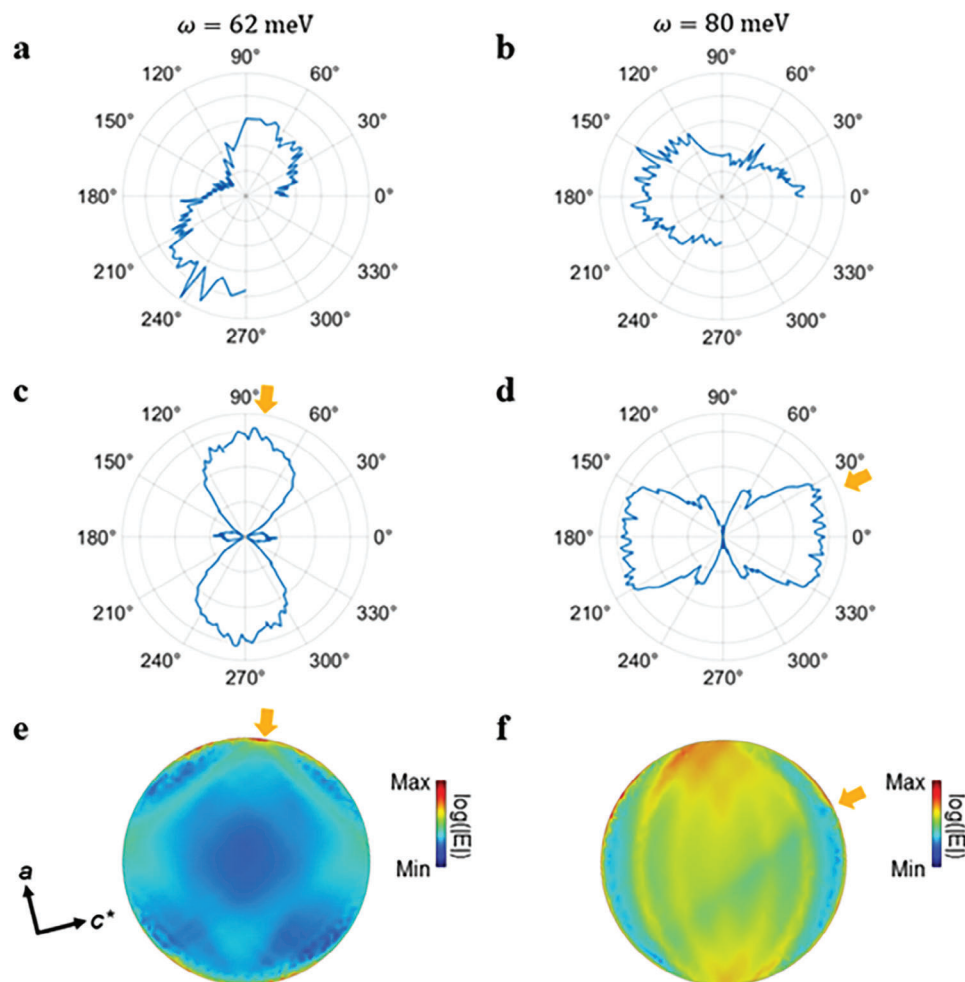


Figure 7. a,b) Polar plots of the EELS intensity at the position adjacent to the edge of the disk in the EELS maps shown in Figure 6b,c, respectively. The data at the lower right quarter of the disk are not drawn on the plot due to the handle of the disk. c,d) Simulation results corresponding to (a) and (b), respectively. The angular positions of the maximum EELS intensity are marked by yellow arrows. e,f) Simulated field distribution at the top surface of the nanodisk at the energy of e) 62 meV and f) 80 meV. The electron beam is placed at the position where the simulated EELS intensity in (c) and (d) show maximum. The angular position of the electron beam are also marked by the yellow arrows. Log scales are used in the colormaps to get a better contrast.

in the experiment to calculate the free charge carrier contribution. Other parameters used in the model are taken from ref.[44] The calculated results can be seen in Figure S1a–d (Supporting Information).

The same method used in ref.[18] are performed to treat the permittivity tensor. By inducing a frequency-dependent angle γ around the axis z , the permittivity tensor can be split into a diagonalized tensor in the rotated coordinate system $[mnz]$, as well as a remaining imaginary off-diagonal term $\text{Im}(\epsilon_{mn})$. The calculated results can be seen in Figure S1e–h (Supporting Information). The methods in ref.[18] are used to smooth the curves and avoid the discontinuities.

EELS Data Acquisition and Imaging Experiment: Nion U-HERMES200 microscope was used to acquire EELS data and HAADF image at 60 kV, which is equipped with both a monochromator and aberration correctors. The EELS data were acquired with convergence semiangle $\alpha = 15$ mrad, and collection semiangle $\beta = 25$ mrad. The energy resolution of EELS was about 8 meV. To achieve a high signal-to-noise ratio, acquisition time of 500 ms per pixel was chosen. HAADF images in the inset of Figure 2a was acquired with convergence semiangle $\alpha = 35$ mrad and collection semiangle $\beta = \approx 80$ –210 mrad operated at 60 kV.

EELS Data Processing: All EELS spectra were processed by MATLAB code written by Ruishi Qi. Raw EELS spectra are first aligned by their normalized cross section. Then, block-matching and 3D filtering (BM3D) algorithms are applied to remove Gaussian noise.[54,55] After normalization by the zero-loss peak (ZLP) intensity, signals with a full width at half maximum (FWHM) of ≈ 5.5 meV can be obtained. By fitting the spectra to a Pearson function in two energy windows, one before and one after the energy loss region, the ZLP can be removed, leaving signals with several energy loss peaks. Finally, Lucy–Richardson deconvolution is employed to ameliorate the broadening effect caused by finite energy resolution while taking the elastic peak as the point spread function. By processing EELS data in the same way to each point in sample space, the line profiles and energy-filtered EELS maps shown in the article can be obtained. A more intuitive flow chart describing the above procedure is shown in Figure S3, Supporting Information.

EELS Simulation: The simulation of EELS line profile in Figure 2d was performed by using FDTD. The detailed principle and methods of FDTD simulation have been demonstrated in the literature.[50] The transformation matrix was added to realize the permittivity tensor with off-diagonal terms. Perfect matched layers were used at the boundary of the simulation

region. The mesh fineness and the size of simulation region were carefully chosen to balance accuracy and efficiency.

Electric Field Simulation: The simulation of electric field distribution was performed by using the commercial software COMSOL Multiphysics. The dielectric function and electric field induced by electron beam were taken from previous reports.^[44,50] Perfect matched layers were added at the boundary of the simulation region. A self-adaption mesh was used to improve accuracy.

Supporting Information

Supporting Information is available from the Wiley Online Library or from the author.

Acknowledgements

The work was supported by the National Key R&D Program of China (No. 2022YFA1206700) and the National Natural Science Foundation of China (Nos. 62104010 and 62374010), Beijing Outstanding Young Scientist Program (No. BJJWZYJH0120191000103), and the Beijing Natural Science Foundation (No. Z200004). The work was supported by High-performance Computing Platform of Peking University. The authors acknowledged Electron Microscopy Laboratory of Peking University for the use of electron microscopes. The authors thanked Prof. Qing Dai, Prof. Xiaoxia Yang, Dr. Xiangdong Guo, Dr. Debo Hu, and Prof. Weikun Ge (Tsinghua University) for their helpful discussions.

Conflict of Interest

The authors declare no conflict of interest.

Data Availability Statement

The data that support the findings of this study are available from the corresponding author upon reasonable request.

Keywords

electron energy loss spectroscopy, phonon polaritons, β -Ga₂O₃

Received: May 30, 2022
Revised: January 23, 2024
Published online:

- [1] J. D. Caldwell, A. V. Kretinin, Y. G. Chen, V. Giannini, M. M. Fogler, Y. Francescato, C. T. Ellis, J. G. Tischler, C. R. Woods, A. J. Giles, M. Hong, K. Watanabe, T. Taniguchi, S. A. Maier, K. S. Novoselov, *Nat. Commun.* **2014**, *5*, 5221.
- [2] S. Dai, Z. Fei, Q. Ma, A. S. Rodin, M. Wagner, A. S. McLeod, M. K. Liu, W. Gannett, W. Regan, K. Watanabe, T. Taniguchi, M. Thiemens, G. Dominguez, A. H. C. Neto, A. Zettl, F. Keilmann, P. Jarillo-Herrero, M. M. Fogler, D. N. Basov, *Science* **2014**, *343*, 1125.
- [3] T. Feurer, N. S. Stoyanov, D. W. Ward, J. C. Vaughan, E. R. Statz, K. A. Nelson, *Ann. Rev. Mater. Res.* **2007**, *37*, 317.
- [4] D. L. Mills, E. Burstein, *Rep. Prog. Phys.* **1974**, *37*, 817.
- [5] D. N. Basov, M. M. Fogler, F. J. G. de Abajo, *Science* **2016**, *354*, aag1992.
- [6] J. D. Caldwell, L. Lindsay, V. Giannini, I. Vurgaftman, T. L. Reinecke, S. A. Maier, O. J. Glembocki, *Nanophotonics* **2015**, *4*, 44.
- [7] Z. Jacob, *Nat. Mater.* **2014**, *13*, 1081.
- [8] T. Low, A. Chaves, J. D. Caldwell, A. Kumar, N. X. Fang, P. Avouris, T. F. Heinz, F. Guinea, L. Martin-Moreno, F. Koppens, *Nat. Mater.* **2017**, *16*, 182.
- [9] L. Tranchant, S. Harnamura, J. Ordonez-Miranda, T. Yabuki, A. Vega-Flick, F. Cervantes-Alvarez, J. J. Alvarado-Gil, S. Volz, K. Miyazaki, *Nano Lett.* **2019**, *19*, 6924.
- [10] Y. Wu, J. Ordonez-Miranda, S. Gluchko, R. Anufriev, D. D. Meneses, L. Del Campo, S. Volz, M. Nomura, *Sci. Adv.* **2020**, *6*, eabb4461.
- [11] J. Martin-Sanchez, J. H. Duan, J. Taboada-Gutierrez, G. Alvarez-Perez, K. V. Voronin, I. Prieto, W. L. Ma, Q. L. Bao, V. S. Volkov, R. Hillenbrand, A. Y. Nikitin, P. Alonso-Gonzalez, *Sci. Adv.* **2021**, *7*, eabj0127.
- [12] N. Li, X. D. Guo, X. X. Yang, R. S. Qi, T. Y. Qiao, Y. F. Li, R. C. Shi, Y. H. Li, K. H. Liu, Z. Xu, L. Liu, F. J. G. de Abajo, Q. Dai, E. G. Wang, P. Gao, *Nat. Mater.* **2021**, *20*, 43.
- [13] W. K. Dong, R. S. Qi, T. S. Liu, Y. Li, N. Li, Z. Hua, Z. R. Gao, S. Y. Zhang, K. H. Liu, J. D. Guo, P. Gao, *Adv. Mater.* **2020**, *32*, 2002014.
- [14] W. L. Ma, P. Alonso-Gonzalez, S. J. Li, A. Y. Nikitin, J. Yuan, J. Martin-Sanchez, J. Taboada-Gutierrez, I. Amenabar, P. N. Li, S. Velez, C. Tollan, Z. G. Dai, Y. P. Zhang, S. Sriram, K. Kalantar-Zadeh, S. T. Lee, R. Hillenbrand, Q. L. Bao, *Nature* **2018**, *562*, 557.
- [15] Z. B. Zheng, J. N. Chen, Y. Wang, X. M. Wang, X. B. Chen, P. Y. Liu, J. B. Xu, W. G. Xie, H. J. Chen, S. Z. Deng, N. S. Xu, *Adv. Mater.* **2018**, *30*, 1705318.
- [16] F. C. B. Maia, B. T. O'Callahan, A. R. Cadore, I. D. Barcelos, L. C. Campos, K. Watanabe, T. Taniguchi, C. Deneke, A. Belyanin, M. B. Raschke, R. O. Freitas, *Nano Lett.* **2019**, *19*, 708.
- [17] H. Salihoglu, V. Iyer, T. Taniguchi, K. Watanabe, P. D. Ye, X. F. Xu, *Adv. Funct. Mater.* **2020**, *30*, 1905830.
- [18] N. C. Passler, X. Ni, G. Hu, J. R. Matson, G. Carini, M. Wolf, M. Schubert, A. Alo, J. D. Caldwell, T. G. Folland, A. Paarmann, *Nature* **2022**, *602*, 595.
- [19] Z. Guo, A. Verma, X. F. Wu, F. Y. Sun, A. Hickman, T. Masui, A. Kuramata, M. Higashiwaki, D. Jena, T. F. Luo, *Appl. Phys. Lett.* **2015**, *106*, 111909.
- [20] H. Y. He, R. Orlando, M. A. Blanco, R. Pandey, E. Amzallag, I. Baraille, M. Rerat, *Phys. Rev. B* **2006**, *74*, 195123.
- [21] H. Y. Playford, A. C. Hannon, E. R. Barney, R. I. Walton, *Chemistry* **2013**, *19*, 2803.
- [22] H. H. Tippins, *Phys. Rev.* **1965**, *140*, A316.
- [23] E. G. Villora, K. Shimamura, Y. Yoshikawa, T. Ujiie, K. Aoki, *Appl. Phys. Lett.* **2008**, *92*, 202120.
- [24] J. Q. Wei, K. Kim, F. Liu, P. Wang, X. T. Zheng, Z. Y. Chen, D. Wang, A. Imran, X. Rong, X. L. Yang, F. J. Xu, J. Yang, B. Shen, X. Q. Wang, *J. Semicond.* **2019**, *40*, 012802.
- [25] J. Q. Wei, F. Liu, X. Rong, T. Wang, L. Y. Yang, R. C. Tao, J. Yang, L. W. Guo, B. Shen, X. Q. Wang, *CrystEngComm* **2022**, *24*, 269.
- [26] J. Furthmuller, F. Bechstedt, *Phys. Rev. B* **2016**, *93*, 115204.
- [27] A. Mock, R. Korlacki, C. Brolley, V. Darakchieva, B. Monemar, Y. Kumagai, K. Goto, M. Higashiwaki, M. Schubert, *Phys. Rev. B* **2017**, *96*, 245205.
- [28] C. Sturm, J. Furthmuller, F. Bechstedt, R. Schmidt-Grund, M. Grundmann, *APL Mater.* **2015**, *3*, 106106.
- [29] M. Higashiwaki, K. Sasaki, T. Kamimura, M. H. Wong, D. Krishnamurthy, A. Kuramata, T. Masui, S. Yamakoshi, *Appl. Phys. Lett.* **2013**, *103*, 123511.
- [30] M. Higashiwaki, K. Sasaki, A. Kuramata, T. Masui, S. Yamakoshi, *Appl. Phys. Lett.* **2012**, *100*, 013504.
- [31] M. Higashiwaki, K. Sasaki, H. Murakami, Y. Kumagai, A. Koukitu, A. Kuramata, T. Masui, S. Yamakoshi, *Semicond. Sci. Technol.* **2016**, *31*, 034001.
- [32] K. Sasaki, A. Kuramata, T. Masui, E. G. Villora, K. Shimamura, S. Yamakoshi, *Appl. Phys. Express* **2012**, *5*, 035502.

- [33] Y. Yuan, W. Hao, W. Mu, Z. Wang, X. Chen, Q. Liu, G. Xu, C. Wang, H. Zhou, Y. Zou, X. Zhao, Z. Jia, J. Ye, J. Zhang, S. Long, X. Tao, R. Zhang, Y. Hao, *Fundam. Res.* **2021**, *1*, 697.
- [34] D. T. Ha, D. T. Thuy, V. T. Hoa, T. T. Van, N. A. Viet, in *41st Vietnam National Conference on Theoretical Physics*, Vol. 865 (Eds: T. X. Hoang, H. A. Tuan, V. N. Tuoc), Iop Publishing Ltd, Bristol **2017**.
- [35] M. Bosman, V. J. Keast, J. L. Garcia-Munoz, A. J. D'Alfonso, S. D. Findlay, L. J. Allen, *Phys. Rev. Lett.* **2007**, *99*, 086102.
- [36] O. L. Krivanek, T. C. Lovejoy, N. Dellby, T. Aoki, R. W. Carpenter, P. Rez, E. Soignard, J. T. Zhu, P. E. Batson, M. J. Lagos, R. F. Egerton, P. A. Crozier, *Nature* **2014**, *514*, 209.
- [37] M. J. Lagos, A. Trugler, U. Hohenester, P. E. Batson, *Nature* **2017**, *543*, 529.
- [38] T. C. Lovejoy, G. C. Corbin, N. Dellby, M. Hoffman, O. L. Krivanek, *Microsc. Microanal.* **2018**, *24*, 446.
- [39] M. Varela, S. D. Findlay, A. R. Lupini, H. M. Christen, A. Y. Borisevich, N. Dellby, O. L. Krivanek, P. D. Nellist, M. P. Oxley, L. J. Allen, S. J. Pennycook, *Phys. Rev. Lett.* **2004**, *92*, 095502.
- [40] Z. Y. Wang, D. Santhanagopalan, W. Zhang, F. Wang, H. L. L. Xin, K. He, J. C. Li, N. Dudney, Y. S. Meng, *Nano Lett.* **2016**, *16*, 3760.
- [41] S. Huang, R. Shi, Y. Li, M. Wu, N. Li, J. Du, D. Yu, P. Gao, *Zhenkong Kexue Yu Jishu Xuebao* **2021**, *41*, 213.
- [42] S. Geller, *J. Chem. Phys.* **1960**, *33*, 676.
- [43] D. L. Rousseau, R. P. Bauman, S. P. S. Porto, *J. Raman Spectrosc.* **1981**, *10*, 253.
- [44] M. Schubert, R. Korlacki, S. Knight, T. Hofmann, S. Schoche, V. Darakchieva, E. Janzen, B. Monemar, D. Gogova, Q. T. Thieu, R. Togashi, H. Murakami, Y. Kumagai, K. Goto, A. Kuramata, S. Yamakoshi, M. Higashiwaki, *Phys. Rev. B* **2016**, *93*, 125209.
- [45] R. S. Qi, R. D. Wang, Y. H. Li, Y. W. Sun, S. L. Chen, B. Han, N. Li, Q. Zhang, X. F. Liu, D. P. Yu, P. Gao, *Nano Lett.* **2019**, *19*, 5070.
- [46] A. C. Peter, *Ultramicroscopy* **2017**, *180*, 104.
- [47] L. A. Giannuzzi, F. A. Stevie, *Micron* **1999**, *30*, 197.
- [48] S. Reyntjens, R. Puers, *J. Micromech. Microeng.* **2001**, *11*, 287.
- [49] A. Losquin, M. Kociak, *ACS Photonics* **2015**, *2*, 1619.
- [50] Y. Cao, A. Manjavacas, N. Large, P. Nordlander, *ACS Photonics* **2015**, *2*, 369.
- [51] Q. Zhang, Q. D. Ou, G. W. Hu, J. Y. Liu, Z. G. Dai, M. S. Fuhrer, Q. L. Bao, C. W. Qiu, *Nano Lett.* **2021**, *21*, 3112.
- [52] Z. G. Dai, G. W. Hu, G. Y. Si, Q. D. Ou, Q. Zhang, S. Balendhran, F. Rahman, B. Y. Zhang, J. Z. Ou, G. G. Li, A. Alu, C. W. Qiu, Q. L. Bao, *Nat. Commun.* **2020**, *11*, 6086.
- [53] R. Lingstadt, N. Talebi, M. Hentschel, S. Mashhadi, B. Gompf, M. Burghard, H. Giessen, P. A. van Aken, *Commun. Mater.* **2021**, *2*, 5.
- [54] K. Dabov, A. Foi, V. Katkovnik, K. Egiazarian, *IEEE Trans. Image Process* **2007**, *16*, 2080.
- [55] J. H. Zhou, Y. S. Yang, Y. Yang, D. S. Kim, A. Yuan, X. Z. Tian, C. Ophus, F. Sun, A. K. Schmid, M. Nathanson, H. Heinz, Q. An, H. Zeng, P. Ercius, J. W. Miao, *Nature* **2019**, *570*, 500.